

CANUCS: UV and Ionising Properties of Dwarf Star Forming Galaxies at $z \sim 5$ to 7

Anishya Harshan,^{1*} Maruša Bradač¹, Roberto Abraham^{2,3}, Yoshihisa Asada^{4,5}, Gabriel Brammer⁶, Guillaume Desprez⁴, Karthiek Iyer⁸, Nicholas S. Martis^{1,4,9}, Jasleen Matharu^{6,7}, Lamiya Mowla¹⁰, Adam Muzzin¹¹, Gaël Noirot⁴, Gregor Rihtaršič¹, Ghassan T. E. Sarrouh¹¹, Marcin Sawicki⁴, Victoria Strait^{6,7}, Chris J. Willott⁹,

¹ Department of Mathematics and Physics, Jadranska ulica 19, SI-1000 Ljubljana, Slovenia

² David A. Dunlap Department of Astronomy and Astrophysics, University of Toronto, 50 St. George Street, Toronto, Ontario, M5S 3H4, Canada

³ Dunlap Institute for Astronomy and Astrophysics, 50 St. George Street, Toronto, Ontario, M5S 3H4, Canada

⁴ Department of Astronomy & Physics and Institute for Computational Astrophysics, Saint Mary's University, 923 Robie Street, Halifax, NS B3H 3C3, Canada

⁵ Department of Astronomy, Kyoto University, Sakyo-ku, Kyoto 606-8502, Japan

⁶ Niels Bohr Institute, University of Copenhagen, Jagtvej 128, DK-2200 Copenhagen N, Denmark

⁷ Cosmic Dawn Center (DAWN), Denmark

⁸ Columbia Astrophysics Laboratory, Columbia University, 550 West 120th Street, New York, NY 10027, USA

⁹ National Research Council of Canada, Herzberg Astronomy & Astrophysics Research Centre, 5071 West Saanich Road, Victoria, BC, V9E 2E7, Canada

¹⁰ Whittin Observatory, Department of Physics and Astronomy, Wellesley College, 106 Central Street, Wellesley, MA 02481, USA

¹¹ Department of Physics and Astronomy, York University, 4700 Keele St. Toronto, Ontario, M3J 1P3, Canada

Accepted XXX. Received YYY; in original form ZZZ

ABSTRACT

The epoch of reionisation progressed through the emission of ionising photons from galaxies to their local intergalactic medium. In this work, we characterise the dwarf star-forming galaxies as candidates for the source of ionising photons that drove EoR. We investigate the ionising properties and star formation histories of star-forming dwarf galaxies at the last stages of EoR at $4.8 < z < 7$ using observations from the CANadian NIRISS Unbiased Cluster Survey (CANUCS). The magnification due to gravitational lensing allows us to probe large dynamic ranges in stellar mass ($2 \times 10^6 \leq M_*/M_\odot \leq 5 \times 10^9$) and UV magnitudes ($-22.68 \leq M_{UV} \leq -15.95$). We find a median UV slope β_{1500} of -2.56 ± 0.23 and the production efficiency of ionising photons $\log \xi_{\text{ion}} = 25.39 \pm 0.6$ for the full sample ($4.8 < z < 7$) with a median stellar mass of $6.3 \pm 0.5 \times 10^7 M_\odot$. We find both β_{1500} and ξ_{ion} are marginally correlated with the stellar mass of the galaxy, indicating a possible greater contribution of dwarf galaxies to the reionisation of the Universe. We find that on average, galaxies in our sample are experiencing a recent rise/burst of star formation which translates to a higher scatter in ξ_{ion} and a large scatter in H α equivalent widths. Finally, we investigate the trends of H α and [OIII]+H β EWs with UV magnitude and find M_{UV} is correlated between H α but not with [OIII]+H β EWs indicating low metallicities and recent burst in the UV faint galaxies.

Key words: Galaxies: high-redshift – Galaxies: evolution – dark ages, reionization, first stars

1 INTRODUCTION

The production of ionising photons is a fundamental process that plays a crucial role in shaping the reionisation history of the Universe. However, the sources of ionizing photons that drove reionisation at redshifts $z > 5.5$ (e.g., Bolan et al. 2021; Davies et al. 2018; McGreer et al. 2014) are poorly understood. Current observational evidence suggests that reionisation proceeded through the escape of ionizing photons from young massive stellar populations in galaxies (see review Robertson (2022) and references within). To ascertain the contribution of different galaxies to reionisation, we need to determine the rate of ionizing photons emitted into the intergalactic medium (IGM) from different galaxy populations. The rate of ion-

izing photons emitted by galaxies can be determined by combining the non-ionising UV luminosity function, escape fraction of ionising photons into the IGM and the ionising photon production efficiency.

The ionising photon production efficiency (ξ_{ion}) is the measure of rate of hydrogen-ionising photon production ($E \geq 13.6$ eV) by young massive stars in a galaxy per unit non-ionising UV continuum luminosity produced on average by the less massive stars. Thus ξ_{ion} should depend on the fraction of massive ionising stars which is regulated by the initial mass function and the star formation history of the galaxy. Along with the escape fraction of ionising photons (f_{esc}), ξ_{ion} is used to determine whether a galaxy is capable of reionising the local IGM. Direct measurement of ξ_{ion} requires detection of ionising Ly-continuum photons emitted by the galaxy which becomes increasingly difficult for high redshift galaxies as the radiation would be absorbed by the intergalactic medium. Thus the measurement of

* E-mail: anishya.thevalil-harshan@fmf.uni-lj.si

ξ_{ion} for high redshift galaxies has exclusively relied on indirect methods. As the bright nebular recombination line $\text{H}\alpha$ (6562Å) is directly related to the total number of Ly-continuum photons produced by stars in a galaxy (assuming an escape fraction of zero : [Leitherer & Heckman 1995](#)), $\text{H}\alpha$ line can be used to constrain ξ_{ion} (e.g., [Bouwens et al. \(2016\)](#); [Chisholm et al. \(2022\)](#); [Stefanon et al. \(2022\)](#); [Prieto-Lyon et al. \(2022\)](#)).

The past decade has seen many studies estimating ξ_{ion} using indirect $\text{H}\alpha$ at $z \sim 4$ to 5 based on stacking Spitzer/IRAC photometry (e.g., [Bouwens et al. \(2016\)](#); [Lam et al. \(2019\)](#); [Stefanon et al. \(2019\)](#)) and at lower redshifts $z \sim 1$ to 3.7, where $\text{H}\alpha$ or $\text{H}\beta$ was observable from ground based telescopes ([Nakajima et al. 2016](#); [Nanayakkara et al. 2020](#); [Matthee et al. 2016](#)). These studies indicate that the ξ_{ion} increases with redshift, and thus the average escape fraction required for galaxies to ionise the local IGM would be $\approx 10 - 20\%$ ([Ouchi et al. 2009](#); [Robertson et al. 2015](#); [Finkelstein et al. 2019](#); [Naidu et al. 2019](#)) at $z = 6$. However, most studies relied on low statistics, lower redshift analogs or wide band photometry and image stacking due to lack of access to Balmer lines. This has been mitigated with the launch of the James Webb Space Telescope (JWST), and we are able to observe Balmer lines using spectroscopy and/or medium/narrow band photometry to accurately measure $\text{H}\alpha$ fluxes. Recently a number of studies using JWST observations like [Lin et al. \(2023\)](#); [Simmonds et al. \(2023\)](#); [Tang et al. \(2023\)](#); [Saxena et al. \(2023\)](#); [Prieto-Lyon et al. \(2022\)](#); [Atek et al. \(2023\)](#); [Mascia et al. \(2023\)](#) have measured ξ_{ion} , however, these studies rely on luminous and/or high mass galaxies or small samples for dwarf galaxies. Thus the ionisation properties of faint, low-mass galaxies remain unclear.

Observational studies suggest that low-mass galaxies should have a high contribution to the reionisation of the Universe because of their abundance indicated by the steep slope at the faint end of the UV luminosity function in the high redshift Universe ([Sawicki & Thompson 2006](#); [Reddy & Steidel 2009](#); [Bouwens et al. 2011](#); [Dressler et al. 2015](#); [Finkelstein et al. 2015](#); [Ishigaki et al. 2015](#); [Livermore et al. 2017](#); [Mehta et al. 2017](#); [Atek et al. 2018](#); [Bhatawdekar et al. 2018](#); [Atek et al. 2023](#)). The same is also suggested by simulation studies like [Balu et al. \(2023\)](#), who suggest that inclusion of low mass halos significantly increases the progression of reionisation. Additionally, owing to the low gravitational potential along with stochastic star formation histories, low stellar mass galaxies are thought to have a higher escape fraction of ionising photons into the local IGM ([Paardekooper et al. 2012](#); [Wise et al. 2014](#); [Erb 2015](#); [Anderson et al. 2017](#); [Karman et al. 2016](#)) at high redshifts. In order to determine the contribution of low-mass galaxies to the reionisation of the Universe, we need to investigate their star formation and ionising properties and compare them to their massive counterparts. However, due to the faintness of low-mass galaxies, most studies have focused on more massive and luminous galaxies.

To that end, we use the CANadian NIRISS Unbiased Cluster Survey ([Willott et al. 2022](#), CANUCS), to study the low mass galaxies at redshift $z > 5$. The magnification provided by the lensing galaxy clusters along with the capabilities of the JWST means we are now able to spectroscopically observe low stellar mass faint galaxies that were previously hidden at $z > 5$. With CANUCS, we are able to reach UV magnitude $M_{\text{UV}} \approx -15.95$ compared to $M_{\text{UV}} \approx -16.4$ from the deep imaging from the JADES ([Eisenstein et al. 2023](#); [Endsley et al. 2023a](#)) for galaxies at $6 < z < 9$. We use medium and broad band photometry from NIRCcam and prism spectroscopy from NIRSspec to study the ionisation properties and star formation histories of star-forming galaxies at $5 < z < 7$. The outline of the paper is as follows: We describe the observations, data reduction, and sample selection in section 2. In section 3, we describe the methodology

followed for flux measurements from photometric and spectroscopic observations, dust correction, and measurements of UV and ionising properties. In section 4, we discuss the results on the UV slope, ξ_{ion} , and emission line equivalent widths and finally summarise our findings in section 5.

We assume a flat Λ CDM cosmology with $\Omega_m = 0.3$, $\Omega_\Lambda = 0.7$, $h = 0.7$, all magnitudes are in the AB system.

2 DATA AND TARGET SELECTION

2.1 Imaging Data

In this work, we use data from the Canadian NIRISS Unbiased Cluster Survey ([Willott et al. 2022](#), CANUCS), a JWST GTO program (Program ID 1208; PI C. Willott) and the HST program 16667 (PI M. Bradač). We select our sample from the observations of the MACS J0417.5-1154 cluster (CLU) field and the respective NIRCcam flanking (NCF) field. In the central CLU field, the CANUCS imaging data consists of HST/ACS filters: F435W, F606W, F814W and JWST/NIRCcam filters: F090W, F115W, F150W, F200W, F277W, F356W, F410M, F444W. In the NCF field we have HST/WFC3 filters: F438M, F606W and JWST/NIRCcam filters: F090W, F115W, F140M, F150W, F162M, F182M, F210M, F250M, F277W, F300M, F335M, F360M, F410M, F444W. CANUCS image reduction and photometry procedure is described in detail in [Noirot et al. \(2023\)](#). In short, we use a modified version of the Detector1 Pipeline (calwebb_detector1) stage of the official STScI pipeline and jwst_0916.pmap JWST Operational Pipeline (CRDS_CTX) to reduce the NIRCcam data. We perform astrometric alignment of the different exposures of JWST/NIRCcam to HST/ACS images, sky subtraction, and drizzling to a common pixel scale of $0.04''$ using version 1.6.0 of the grism redshift and line analysis software for space-based spectroscopy ([Brammer & Matharu 2021](#), Grizli). The source detection and photometry is done with the Photutils package ([Bradley et al. 2022](#)) on the χ_{mean} detection image created using all available images. For each detected source, total fluxes are measured in elliptical apertures based on the Kron radius and circular apertures of diameter $0.3''$ and $0.7''$ ([Asada et al. 2024](#)). In this work, we use $0.7''$ -diameter aperture photometry on HST/ACS and JWST/NIRCcam images that were PSF-homogenized to the resolution of the F444W data ([Sarrouh et al., in prep](#)). We calculate the photometric redshifts using EAZY-py ([Brammer et al. 2008](#); [Brammer 2023a](#)) with SED templates from [Larson et al. \(2022\)](#) that are based on FSPS ([Conroy & Gunn 2010](#)) and BPASS ([Eldridge et al. 2017](#)) stellar population synthesis models and CLOUDY ([Ferland et al. 2017](#); [Byler 2018](#)) photoionization code.

We select our photometric sample between redshift 4.8 and 5.5 such that the medium band F410M of JWST/NIRCcam includes flux from the $\text{H}\alpha$ (6562Å) emission line creating a flux excess. We get a sample of 270 objects with flux excess in F410M (i.e., $\text{Flux}_{\text{F410M}} > \text{Flux}_{\text{F444W}}$) in the selected redshift range. We impose SNR cuts for Lyman-break dropout ($\text{SNR}_{\text{F606W}} < 2$ and $\text{SNR}_{\text{F090W}} > 3$) and visually inspect each object and select our final sample of 156 galaxies. We refer to this sample as the NIRCcam sample throughout the paper.

2.2 Spectroscopic Data

Galaxies selected with excess flux in F410M and Lyman break dropout in F606W, F814W or F090W were selected for spectroscopic follow-up without imposing a magnitude limit with JWST/NIRSspec

micro-shutter assembly in the low-resolution Prism mode. Our NIRSpec data has been reduced using the JWST pipeline for stage 1 corrections and then the `msaexp` (Brammer 2023b) to create wavelength calibrated, background subtracted 2D spectra. The 1D spectrum is then created for each line by collapsing the spectrum in the spatial axis and extracting the 1D spectrum within 3σ of the peak of the collapsed spectrum. From the CANUCS spectroscopic observations, we confirm a sample of 33 galaxies with $H\alpha$ emission line at $4.8 < z < 7$.

The wavelength coverage of the NIRSpec prism allows for observation of $H\alpha$ emission at $4.8 < z < 7$. Thus, our NIRSpec data covers a higher redshift range compared to our NIRCам sample which covers $4.8 < z < 5.5$. The NIRCам data is limited in wavelength to allow for accurate measurement of $H\alpha$ flux, which can be achieved when $H\alpha$ emission falls in the F410M band (in $4.8 < z < 5.5$). The lower observational depth of the spectroscopic data compared to the NIRCам imaging leads to a sample of lower magnification uncorrected M_{UV} of -24.37 to -18.45 with median $M_{UV} = -20.95 \pm 1.15$ in our NIRSpec Sample compared to uncorrected the M_{UV} range of -23.13 to -18.10 with median $M_{UV} = -20.56 \pm 0.85$ in our NIRCам Sample. Similarly, the magnification uncorrected stellar masses of the NIRSpec sample is in the range $7.78 < \log M_*/M_\odot < 9.51$ with a median $\log M_*/M_\odot = 8.11 \pm 0.42$ compared to the $\log M_*/M_\odot$ range $7.67 < \log M_*/M_\odot < 9.75$ with a median $\log M_*/M_\odot = 8.04 \pm 0.38$ for the NIRCам sample. The properties of the two sample sets are presented in Table 1 and shown in Figure 1.

3 METHODS

3.1 SED fitting and Flux Measurements

We calculate the photometric redshifts using EAZY-Py (Brammer et al. 2008; Brammer 2023a) including SED templates from Larson et al. (2022) that are better suited to fit the SEDs of blue high redshift ($5 < z < 8$) galaxies. We used Dense Basis (Iyer & Gawiser 2017; Iyer et al. 2019) SED fitting code to determine other physical properties of galaxies: stellar masses, star formation rates (SFRs), metallicities, stellar dust attenuation and non-parametric star formation histories (SFHs). Dense Basis uses Flexible Stellar Population Synthesis (FSPS) code (Conroy & Gunn 2010) which includes a prescription for nebular emission from CLOUDY (Ferland et al. 2017; Byler 2018). We adopt the Calzetti et al. (2000) dust model and assume Chabrier (2003) IMF. We fit the photometry from 3 HST/ACS bands and 8 JWST/NIRCам bands covering a wavelength range of $0.4 \mu\text{m}$ to $4 \mu\text{m}$ for the CLU field and 2 HST/WFC3 bands and 14 JWST/NIRCам bands for the NCF field covering a wavelength range of $0.4 \mu\text{m}$ to $4 \mu\text{m}$. The photometric sample is selected with $H\alpha$ flux excess in the F410M medium band and has been visually inspected to be a Lyman-continuum drop-out in the F606W or F814W bands. Thus, we run Dense Basis with uniform redshift prior in $4.7 < z < 6$ range. For the spectroscopic sample, we fix the redshift at the measured spectroscopic redshift while running Dense Basis. We use flat stellar mass prior between $5 < \log M_*/M_\odot < 12$, flat sSFR prior between $-12 < \text{sSFR} (\text{yr}^{-1}) < -7$, varied metallicity in the range $-2.5 < \log(Z/Z_\odot) < 0.25$ and used an exponential prior for dust attenuation. We then correct the stellar mass, SFR, and SFHs for magnification from gravitational lensing from the foreground cluster. The magnification coefficients are calculated using an updated lens model for MACS0417 (Desprez 2024, in prep.) created with Lenstool (Kneib et al. 1993; Jullo et al. 2007). The model improves upon the Mahler et al. (2019) model by adding several new spectroscopically confirmed multiply imaged systems.

Figure 1 shows the stellar mass distributions before and after magnification corrections. Our sample shows (not corrected for magnification) a lower limit of $\log M_*/M_\odot = 7.3$ (orange unfilled histogram, left) for the NIRCам sample and $\log M_*/M_\odot = 7.78$ (purple unfilled histogram, left) for the NIRSpec sample. After correcting for magnification from gravitational lensing from the cluster, the stellar mass sample ranges between $6.36 < \log M_*/M_\odot < 9.76$ with median $\log M_*/M_\odot = 7.88 \pm 0.57$ and $6.69 < \log M_*/M_\odot < 9.21$ with median $\log M_*/M_\odot = 7.94 \pm 0.53$ for the NIRCам and NIRSpec samples respectively shown in filled histograms in 1. In our sample, the median lensing magnification is 3 ± 1 . Given the distance of the NCF field from the cluster center, we assume a magnification of 1.

We measure the $H\alpha$ flux from the photometry by following the two-filter method and the three-filter method described in Vilella-Rojo et al. (2015) for the CLU and NCF field respectively. In the CLU field, we use the F444W broad band filter to describe the stellar continuum and the F410M medium band with flux excess from $H\alpha$ ($4.8 < z < 5.5$). In the NCF field, we calculate the continuum with the F360M medium band filter and the F444W broad band filter and use the F410M medium band that contains the $H\alpha$ flux. Similarly, only in the NCF field, we calculate the [OIII]+ $H\beta$ flux for the NIRCам sample using the F300M, F335M, and F360M bands. We do not calculate the [OIII]+ $H\beta$ flux for galaxies in the CLU field as the [OIII]+ $H\beta$ falls in the F277W and F356W broad bands for the NIRCам sample which would include spectral features like [OII], Balmer break, etc. We calculate the restframe equivalent width (EW) for each emission line measurement using the extracted emission line following Vilella-Rojo et al. (2015). We bootstrap the photometry within the photometric errors and measure the line fluxes and restframe EWs. We take the median values and 1σ of the distribution as the measured line flux and EWs and associated errors.

For our NIRSpec data, we use the ID spectra and correct for slit loss by performing a spline interpolation of the ratio of mock photometry from the 1D spectrum and the observed photometry and smoothing the interpolated function. For the spline interpolation, we also ignored the photometric bands where the mock photometry from the NIRSpec spectrum was less than 2 SNR. We then extract the 1D spectrum in 200 \AA wavelength windows around emission lines $H\alpha$, [OIII], and $H\beta$ and subtract the local continuum if present. Fluxes and accurate redshifts are then calculated by fitting Gaussian curves on the emission line without putting constraints on the width of the Gaussian. We bootstrap the spectrum with the error spectrum and calculate fluxes. The median flux and redshift and the 1σ of the distribution of the bootstrap are taken as the measured values and associated errors. Given the low resolution of the spectroscopic data from the NIRSpec prism, we note that the $H\alpha$ emission may have contamination from [NII](6585 \AA) emission, and the [OIII] (5007,4959 \AA) doublet is not always fully resolved (depending on SNR). Cameron et al. (2023) found no significant observation of [NII] in deep observation of Lyman break galaxies in $z \sim 5.5 - 9.5$. Thus we assume a negligible contribution of [NII] to the measured $H\alpha$ flux. We follow a similar assumption while calculating $H\alpha$ flux from the medium band photometry. However, we note that if we are to assume $\approx 10\%$ contribution of [NII] as is observed at $z \sim 2$ (Coil et al. 2014; Alcorn et al. 2019), our $H\alpha$ fluxes and quantities measured with $H\alpha$ fluxes will be lowered by $\approx 10\%$. Figure 2 shows reasonable agreement ($< 7\%$ difference) between the $H\alpha$ flux measured with photometric data vs spectroscopy. We note that this comparison has been done within the overlapping NIRCам+NIRSpec sample (at $4.8 < z < 5.5$).

Sample	z	$\log M_*/M_\odot$	M_{UV}	β_{1500}	ξ_{ion}
NIRCam	5.15 ± 0.2 (4.8 - 5.5)	7.8 ± 0.5 (6.3 - 9.7)	-20.0 ± 1.2 (-22.7 - -15.9)	-2.58 ± 0.2 (-3.15 - -0.83)	25.36 ± 0.04 (24.26 - 26.37)
NIRSpec	5.5 ± 0.6 (4.8 - 7)	7.9 ± 0.5 (6.7 - 9.2)	-20.1 ± 1.2 (-21.8 - 17.0)	-2.48 ± 0.4 (-2.78 - -1.73)	25.48 ± 1.0 (21.25 - 26.75)

Table 1. Summary of median values and ranges (in parantheses) of physical properties of the NIRCam and NIRSpec sample. Stellar mass ($\log M_*/M_\odot$), UV magnitude (M_{UV}) are corrected for magnification.

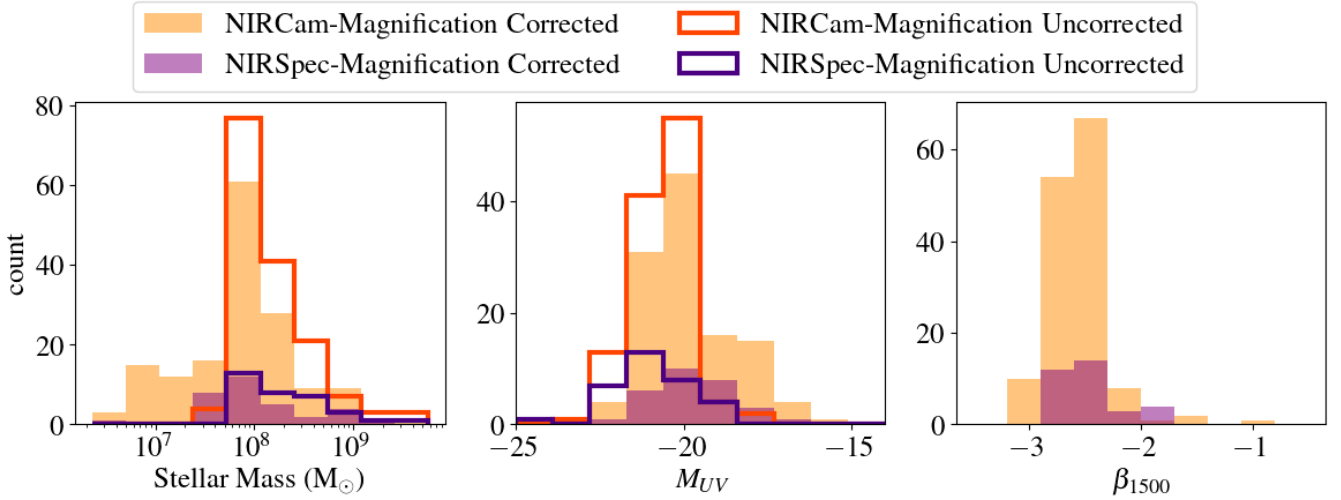


Figure 1. Distribution of Stellar mass (left), UV Magnitude in AB system (center) and the UV slope at 1500 Å (right) for our selected sample. The orange histograms represent the NIRCam sample at redshift $4.8 > z > 5.5$, the violet histograms represent the NIRSpec sample at $4.8 > z > 7$. The filled and unfilled histograms represent the magnification corrected and uncorrected quantities respectively. Gravitational lensing correction improves our detection limits by 1 dex in $\log M_*/M_\odot$ and 2.1 dex in M_{UV} .

3.2 UV Luminosity and UV continuum slope

We measure the UV luminosity of galaxies in the NIRCam sample using filters covering rest-frame 1400–1600 Å. Thus we use F090W for galaxies between the redshift range of 4.8 to 5.5 which avoids the Lyman break and Lyman α emission. For the spectroscopic sample, we use the slit loss corrected 1D spectrum and calculate the UV luminosity in the wavelength window containing 1500 Å determined by the F090W or F115W for each object depending on the redshift. We correct the measured UV luminosity for both photometric and spectroscopic data for lensing magnification. Finally, we bootstrap the measurements within observational errors and report the median values and 1σ errors. Figure 2 compares the UV luminosity measured using photometric and spectroscopic data. We find reasonable agreement between the UV luminosity measured with the two methods with the relative difference being 0.11 ± 0.45 .

We calculate β_{1500} from the model SED from EAZY SED fitting of the observed photometry. We measure β_{1500} by fitting model SED between rest-frame 1400–2000 Å with a single power law in the wavelength windows defined by Calzetti et al. (1994) to avoid absorption and emission lines. β_{1500} measured with EAZY SED fitting is highly dependent on the templates. The inclusion of the Larson et al. (2022) improves the measurement of β_{1500} by increasing the range to reach up to $\beta_{1500} = -3.1$.

Figure 1 shows the UV magnitude and β_{1500} distributions before and after magnification corrections. Our sample shows a lower limit (before magnification correction) of $M_{UV} = -18.1$ (orange un-

filled histogram, center) for the NIRCam sample and $M_{UV} = -18.45$ (purple unfilled histogram, center) for the NIRSpec sample. After correcting for magnification from lensing from the cluster, the UV magnitude ranges between $-22.68 < M_{UV} < -15.95$ with median $M_{UV} = -20.07 \pm 1.27$ and $-21.7 < M_{UV} < -17.01$ with median $M_{UV} = -20.1 \pm 1.17$ for the NIRCam and NIRSpec samples respectively (filled histograms in 1, center). Given the achromatic nature of lensing, β_{1500} is not affected by lensing magnification. The distribution of β_{1500} shows a median $\beta_{1500} = -2.58 \pm 0.26$ for the NIRCam sample and a median $\beta_{1500} = -2.48 \pm 0.42$ in the NIRSpec sample. After figure 1, we only present magnification corrected quantities.

3.3 Dust Correction

The measured $H\alpha$ fluxes are corrected for nebular dust attenuation to account for the light absorbed by dust in the star forming regions in the galaxy. The Balmer decrement ($H\alpha/H\beta$) is one of the most robust ways to correct for nebular dust attenuation. To calculate the intrinsic $H\alpha$ luminosity for our spectroscopic sample, we determine the dust attenuation towards $H\alpha$ by calculating the Balmer color excess following the Case B recombination value (Osterbrock 1989).

$$E(H\beta - H\alpha) = 2.5 \log \left(\frac{H\alpha/H\beta}{2.86} \right)$$

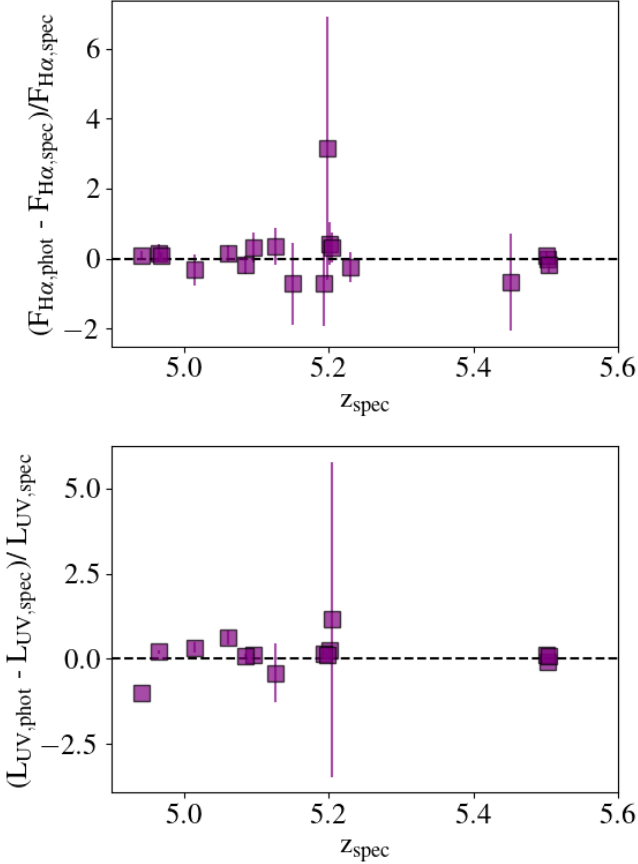


Figure 2. Comparison of $H\alpha$ flux (top), and UV Luminosity (bottom) measured from photometry and spectroscopic data. Our photometric measurements of $H\alpha$ flux (from F410M) and L_{UV} (from F090W) are consistent with the spectroscopic measurements.

Following the Calzetti dust law (Calzetti et al. 2000), the intrinsic $H\alpha$ luminosity is determined as:

$$L_{H\alpha,int} = 10^{0.4A(H\alpha)} \times L_{H\alpha,obs}$$

$$A(H\alpha) = 6.6 \log \left(\frac{H\alpha/H\beta}{2.86} \right)$$

For our photometric sample, where we do not have measurements of $H\beta$ flux to determine the balmer decrement, we use the total attenuation (A_V) determined using Dense Basis SED fitting to calculate the attenuation towards $H\alpha$ luminosity. For our sample, we calculate the median $A_V = 0.11^{+0.04}_{-0.06}$. We adopt the Calzetti dust law following the recent results from Markov et al. (2024), who find the dust law for galaxies at $z > 4.5$ is comparable to the Calzetti dust law. Following Calzetti dust law (Calzetti et al. 2000), attenuation towards $H\alpha$ is determined as:

$$A(H\alpha) = 0.82 \times A_V$$

Given the dust attenuation is higher in the UV wavelengths, the observed UV luminosity in both photometric and spectroscopic data is similarly corrected to determine the intrinsic UV luminosity using the Calzetti dust law at $\lambda = 1500\text{\AA}$ as:

$$A(1500) = 2.55 \times A_V$$

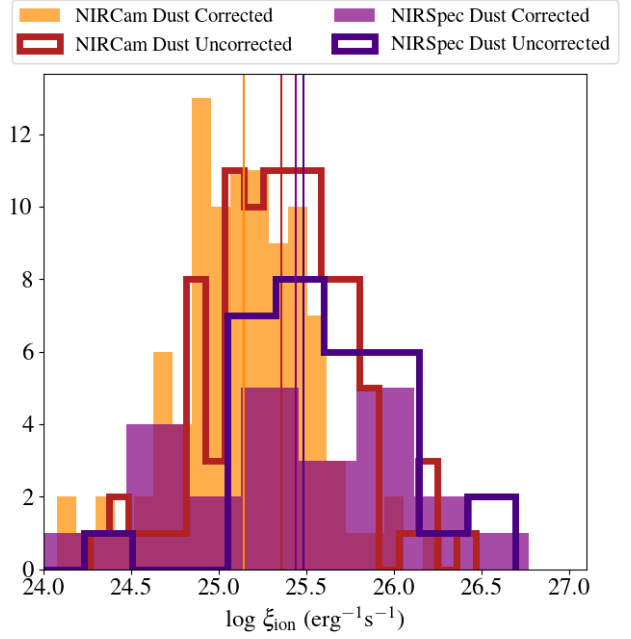


Figure 3. The distribution of ξ_{ion} corrected and uncorrected for dust obscuration is shown in unfilled and filled histograms respectively. The dust correction follows Calzetti et al. (2000) dust law for the NIRCam sample (orange) and using Balmer decrement in the NIRSpec sample (purple). The NIRSpec sample shows no significant difference in the median of the distribution but a slight increase in the σ of the distribution. The NIRCam sample shows a lower median ξ_{ion} in the dust corrected sample by ~ 0.2 dex.

3.4 ξ_{ion} Measurement

Lyman-continuum photon production efficiency in the presence of a non-zero $f_{esc,LyC}$ is used to determine the contribution of an object in ionising the IGM. Since the precise value of $f_{esc,LyC}$ is uncertain, we assume a $f_{esc,LyC} = 0$. From indirect measurements of f_{esc} , studies find median predicted $f_{esc,LyC} < 0.2$ at $6 < z < 9$ (Mascia et al. 2023; Saxena et al. 2023).

Leitherer & Heckman (1995) found the following relation between the $H\alpha$ luminosity and the intrinsic Lyman-continuum photons production rate computed for dust free Case B recombination (Osterbrock 1989) assuming no escape of ionizing photons:

$$L(H\alpha) [\text{ergs}^{-1}] = 1.36 \times 10^{-12} N_{(H_0)} [s^{-1}].$$

Thus, we express $\xi_{ion,0}$ as the ratio of the Lyman-continuum photons production rate to the intrinsic rest-frame UV luminosity (L_{UV}) as:

$$\xi_{ion,0} = \frac{\dot{N}_{(H_0)}}{L_{UV}}$$

We show the distribution of dust corrected and uncorrected $\log \xi_{ion}$ for the NIRCam and NIRSpec samples in figure 3. We find that for our NIRCam sample on average, dust corrected ξ_{ion} is 0.20 dex lower than the uncorrected ξ_{ion} . We note that for this sample we do not have information on the Balmer decrement. In our NIRSpec sample, for which we have the Balmer decrement, the dust corrected ξ_{ion} is < 0.1 dex higher than the uncorrected ξ_{ion} . Similarly, if we assume SMC-like dust attenuation, dust corrected ξ_{ion} is 0.2 and 0.1 dex lower in the NIRCam and NIRSpec samples respectively. Due to the lack of significant effect of dust on the median ξ_{ion} , we report the dust uncorrected ξ_{ion} in the paper.

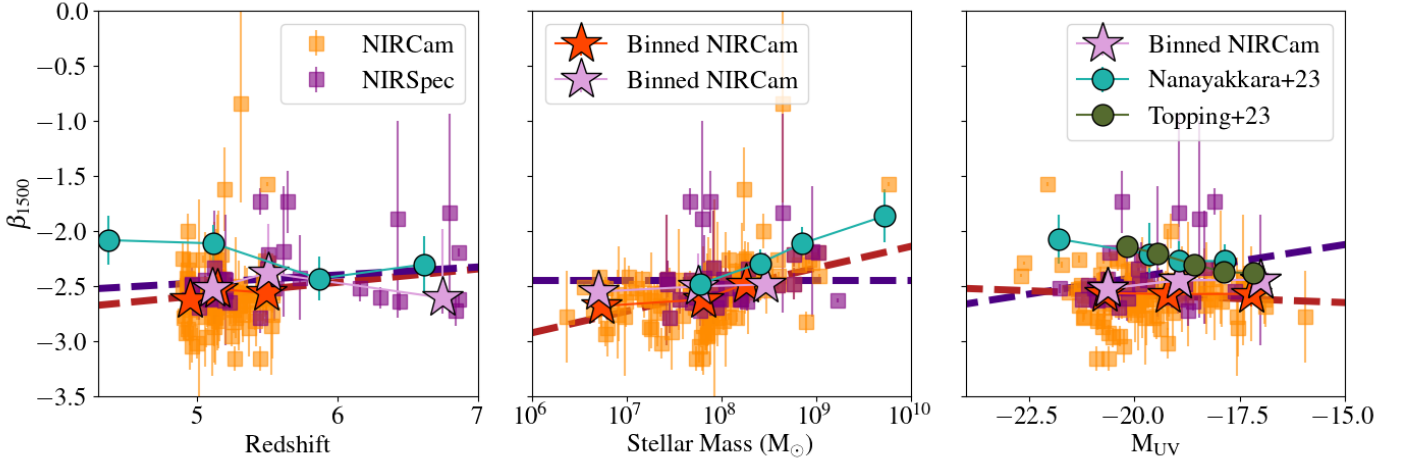


Figure 4. UV continuum slope (β_{1500}) vs redshift (left), stellar mass (center) and M_{UV} (right). Stars show the binned sample and the dashed lines show the linear fit to the full sample. Within the uncertainties, we find no significant correlation between β_{1500} and redshift or M_{UV} . However, we do find a moderate correlation between the β_{1500} and stellar mass in our samples.

4 RESULTS

4.1 The UV slope

The UV continuum slope (β_{1500}) of a galaxy traces the light emitted by young massive stars thus is crucial to constrain the stellar population and star formation history of a galaxy. β_{1500} is dependent on the ages, metallicities, and dust content in a galaxy (Duncan & Conselice 2015; Reddy et al. 2018). Given its dependence on the dust content of the galaxy, β_{1500} is often used to constrain the dust attenuation of the spectrum where Balmer decrement or infrared spectrum is not observed. However, intrinsically, for a dust corrected spectrum, the β_{1500} is dependent on the fraction of very young and metal-poor stellar population. Specifically, young and metal-poor stellar populations result in bluer β_{1500} compared to older metal-rich stellar populations. Given that the main source of ionising UV radiation in a star forming galaxy is from the young massive stellar population, the production efficiency of ionising UV radiation (ξ_{ion}) is expected to correlate with the β_{1500} . In this section, we study the distribution and the evolution of β_{1500} with galaxy properties.

In section 3.2 we describe the method we have adopted to measure β_{1500} for the NIRCam samples. In figure 1, we present the distribution of β_{1500} with 156 galaxies in the photometric (orange). We find $-3.15 < \beta_{1500} < -0.83$ with the median at $\beta_{1500} = -2.56 \pm 0.26$ in the photometric sample. In figure 4, we plot β_{1500} as a function of redshift, stellar mass, and M_{UV} for both the NIRCam (orange) and NIRSpec (purple) samples. The binned sample along with the linear regression between β_{1500} and redshift, stellar mass, and M_{UV} are also shown.

Redshift Evolution of β_{1500} : We find no significant evolution of β_{1500} with the redshift in the NIRCam sample (slope: 0.12, Spearman Coefficient: 0.10). However, we note that our NIRCam sample is restricted to a short range of redshift between $4.8 < z < 5.5$. In our NIRSpec sample, the linear regression measures a slope of 0.07 with a large scatter. Thus we do not find a significant correlation between β_{1500} and z . This overall trend is comparable to the results in the literature (Topping et al. 2023; Nanayakkara et al. 2023; Jiang et al. 2020; Bouwens et al. 2014). We note a large scatter in our sample and a lower correlation compared to the empirical relation of β_{1500} with redshift shown by Bouwens et al. (2014). We also note that

previous studies like Jiang et al. (2020) are unable to recover $\beta_{1500} < -2.6$ with SED fitting due to the limitations of the then available templates, whereas β_{1500} calculated using broad band photometry at high redshift (Bouwens et al. 2014) are affected by the uncertainties in redshifts as well as spectral features.

Correlation of β_{1500} with Stellar Mass: In the middle panel of figure 4, we present the correlation of β_{1500} with the stellar mass of the galaxy. The stellar mass (magnification corrected) in our NIRCam sample ranges from $\log M_*/M_\odot = 6.3$ to 9.75. We find a moderate correlation of β_{1500} with the magnification corrected stellar mass of the galaxies in both our NIRCam sample such that β_{1500} gets shallower with increasing stellar mass. The linear regression of β_{1500} with stellar mass for the NIRCam sample gives a slope of 0.19 and a Spearman coefficient of 0.46, and a slope of 0.007 with low significance in the NIRSpec sample. In the NIRCam sample, the lower mass sample of $\log M_*/M_\odot < 8$ (median = 7.76 ± 0.04) has a $\beta_{1500} = -2.62 \pm 0.02$ compared to $\beta_{1500} = -2.46 \pm 0.04$ in the higher mass sample $\log M_*/M_\odot \geq 8$ (median = 8.26 ± 0.05). The bluer β_{1500} of low mass galaxies implies that the low mass galaxies could have lower dust content, possible higher fraction of ionising radiation, or lower metallicities compared to high mass galaxies. Bluer β_{1500} is also associated with high escape fraction (Chisholm et al. 2022; Mascia et al. 2023), indicating a higher escape fraction in low mass galaxies and thus a higher contribution of low stellar mass galaxies during the epoch of reionisation. This result is comparable to Nanayakkara et al. (2023) who found a correlation between β_{1500} and the stellar mass of galaxies at $4 < z < 8$ similar to our NIRCam sample. We also note that the β_{1500} calculated in Nanayakkara et al. (2023) follows a similar procedure to measure β_{1500} as our NIRCam sample but they do not perform magnification correction for the stellar mass.

Correlation of β_{1500} with UV Magnitude: Finally, we present the correlation of UV magnitude to the β_{1500} in the right panel in figure 4. For our sample with UV magnitude $M_{UV} < -19$, we find a median $\beta_{1500} = -2.58 \pm 0.02$ and for the fainter sample $M_{UV} > -19$, we median find $\beta_{1500} = -2.54 \pm 0.02$. In our NIRCam sample, we do not observe a significant UV magnitude evolution of the β_{1500} (with slope = -0.01 and the Spearman coefficient = -0.02). Similarly, in the NIRSpec sample, we do not observe a significant UV magnitude

evolution of the β_{1500} with slope = 0.05 and Spearman coefficient = 0.03.

We find correlation presented in [Nanayakkara et al. \(2023\)](#) and [Bouwens et al. \(2014\)](#) for a sample at $z = 4$ to 7, and [Topping et al. \(2023\)](#) for a sample at $z = 5$ to 7 comparable to our NIRCam sample, albeit with a shallower slope of the linear fit. The binned median β_{1500} in [Nanayakkara et al. \(2023\)](#) from the GLASS JWST survey at a given UV magnitude is higher compared to our NIRCam sample. However, this discrepancy could be explained by the photometric redshift selection of galaxies in [Nanayakkara et al. \(2023\)](#), whereas we have an additional condition of F410M flux excess from $H\alpha$ emission which biases our sample towards actively star forming galaxies. Similarly, [Topping et al. \(2023\)](#), who calculate β_{1500} directly from photometry also have higher median β_{1500} values at UV magnitude $M_{UV} < -19$ which could be driven by the Lyman break selection. However, previous studies like [Yamanaka & Yamada \(2019\)](#) find an opposite correlation between β_{1500} and M_{UV} in the range $(-22 > M_{UV} > -20)$ at $z \sim 4$. The Lyman break selected galaxies in [Yamanaka & Yamada \(2019\)](#) are possibly biased towards higher dust content.

4.2 Ionising Photon Production Efficiency ξ_{ion}

Constraining ξ_{ion} during the epoch of reionisation for different galaxy populations is important to understand the contribution of different galaxies to EoR and to understand how the reionisation of the Universe proceeded. In this section we explore the evolution of ξ_{ion} with redshift and other galaxy properties at $z \sim 4.8$ to 7 in our NIRCam and NIRSpec samples.

4.2.1 Evolution of ξ_{ion}

We calculate the median ξ_{ion} of $H\alpha$ selected NIRCam sample in the redshift range $4.8 < z < 5.5$ $\log \xi_{ion} = 25.36 \pm 0.40$ compared to the NIRSpec sample in the same redshift range with $\log \xi_{ion} = 25.42 \pm 0.3$. In this redshift range, we find comparable results (within 1σ) between our NIRCam and NIRSpec samples. Whereas, the median ξ_{ion} for galaxies in the NIRSpec sample in redshift range $5.5 < z < 7$ is $\log \xi_{ion} = 25.5 \pm 0.2$ which is higher than the median ξ_{ion} at $4.8 < z < 5.5$ by $< 1\sigma$.

We put in context our measurements by comparing with $H\alpha$ emitters at $4 < z < 4.5$ from [Faisst et al. \(2019\)](#), Lyman-break galaxies at $4 < z < 6$ from [Bouwens et al. \(2016\)](#), [OIII] emitters at $5 < z < 9$ from [Matthee et al. \(2023\)](#), [Tang et al. \(2023\)](#) and [Mascia et al. \(2023\)](#) (also $H\alpha$ and Ly α emitters), and Lyman-alpha emitters (LAEs) at $z > 4$ from [Lam et al. \(2019\)](#), [Ning et al. \(2022\)](#), [Simmonds et al. \(2023\)](#) and [Saxena et al. \(2023\)](#). Among these, [Matthee et al. \(2023\)](#), [Tang et al. \(2023\)](#) and [Saxena et al. \(2023\)](#) measure Balmer line fluxes directly from spectroscopy and [Bouwens et al. \(2016\)](#), [Faisst et al. \(2019\)](#), [Lam et al. \(2019\)](#), [Ning et al. \(2022\)](#) and [Simmonds et al. \(2023\)](#) make measurements from photometry.

The median $\log \xi_{ion} = 25.36 \pm 0.04$ at $4.8 < z < 5.5$ in our photometric sample is comparable to the median $\log \xi_{ion} = 25.27 \pm 0.03$, 25.5 , 25.36 ± 0.08 reported in [Bouwens et al. \(2016\)](#), [Faisst et al. \(2019\)](#) and [Lam et al. \(2019\)](#) at similar redshifts. At $z \sim 6$, ξ_{ion} from [Ning et al. \(2022\)](#) and [Simmonds et al. \(2023\)](#) (median $\log \xi_{ion} = 25.48 \pm 0.4$ and $25.44^{+0.21}_{-0.15}$ respectively) are also comparable to our ξ_{ion} at $z < 5.5$. At $5.5 < z < 7$, the median $\log \xi_{ion}$ of $= 25.6 \pm 0.2$ in our NIRSpec sample is comparable to $\log \xi_{ion} = 25.3$, 25.8 ± 0.09 and 25.56 at $6 < z < 8$ reported in [Matthee et al. \(2023\)](#), [Tang et al. \(2023\)](#) and [Saxena et al. \(2023\)](#).

From our NIRSpec sample, we confirm that 4 out of 33 galaxies are Ly α emitters (LAE) with median $\log \xi_{ion} = 25.49 \pm 0.17$ compared to the median $\log \xi_{ion} = 25.48 \pm 0.2$ of the non-LAE. We find no significant difference between the ξ_{ion} of LAE and non-LAE in our NIRSpec sample. We also find no significant difference between LAE reported in [Lam et al. \(2019\)](#), [Ning et al. \(2022\)](#), [Simmonds et al. \(2023\)](#), and [Saxena et al. \(2023\)](#) and the non-LAE in our sample. The lack of significant difference between ξ_{ion} in the LAE and non-LAE also indicates different physical processes driving the production of ionising photons and creating channels of escape for Lyman α photons in different galaxies similar to the findings in [Saxena et al. \(2023\)](#).

Overall, we find marginal evolution of median ξ_{ion} between our sample and median ξ_{ion} reported in the literature between $4 < z < 9$. At $z < 5.5$. Median $\log \xi_{ion} = 25.36 \pm 0.04$ and $\log \xi_{ion} = 25.48 \pm 1$ for our NIRCam and NIRSpec sample respectively is lower ($< 1\sigma$) than 25.8 ± 0.09 and 25.56 reported in [Tang et al. \(2023\)](#) and [Saxena et al. \(2023\)](#). However, it is consistent with $\log \xi_{ion} = 25.36 \pm 0.07$ and 25.3 in [Mascia et al. \(2023\)](#) and [Matthee et al. \(2023\)](#) respectively. We note that the selection of $H\alpha$ emitters for our sample biases the sample towards higher ξ_{ion} compared to a LBG selection that is done in the stated literature studies and we might miss galaxies with low ξ_{ion} . We also find a large scatter in ξ_{ion} , especially in the NIRCam sample, which indicates a stochastic star formation in galaxies at $z > 5$.

4.2.2 ξ_{ion} vs Stellar Mass and Star Formation

The dependence of the production of ionising photons on the young and massive stellar population in a galaxy indicates that ξ_{ion} should show a correlation with the stellar mass and the star formation history of a galaxy. In this section, we explore the evolution of ξ_{ion} with the stellar mass and star formation history of the galaxies.

Figure 6 shows ξ_{ion} as a function of magnification-corrected stellar mass and the specific star formation rates calculated from Dense Basis SED fitting of the NIRCam (orange squares) and NIRSpec sample (purple squares). The NIRCam sample covers a range of magnification corrected $\log M_*/M_\odot = 6.3 - 9.8$ and the NIRSpec sample covers the range of $\log M_*/M_\odot = 7.2 - 9.1$. We further bin the sample into 5 stellar mass bins of $\log M_*/M_\odot = 6.3 - 7$, $7 - 7.5$, $7.5 - 8$, $8 - 8.5$ and > 8.5 . The stars show the median ξ_{ion} and the median stellar mass of the binned sample. We find that ξ_{ion} decreases marginally (by ~ 0.12 dex) with increasing stellar mass such that the median $\log \xi_{ion} = 25.57 \pm 0.06$ for galaxies with $\log M_*/M_\odot < 7$ and $= 25.46 \pm 0.1$ for $\log M_*/M_\odot > 8$. The linear fit also shows a negative slope of -0.16 and -0.28 for the NIRCam and NIRSpec samples respectively. Although the negative slopes indicate a moderate negative correlation between ξ_{ion} and the stellar mass of the galaxy, we note that the intrinsic scatter of the ξ_{ion} measurement is large at standard deviation $1\sigma = 0.40$ for the NIRCam sample and $1\sigma = 1.03$ for the NIRSpec sample. Further, we calculate the Spearman correlation coefficient. We find a negative correlation coefficient of -0.03 for the NIRCam sample and -0.21 for the NIRSpec sample. Our NIRSpec sample indicates a slight negative correlation of ξ_{ion} with the stellar mass of the galaxies within a large intrinsic scatter, however, the Spearman correlation finds no significant correlation between ξ_{ion} and stellar mass in our NIRCam sample.

Given the difficulty in observing faint low stellar mass galaxies at $z \geq 5$, which has only recently been made available with the launch of JWST, similar results have been reported in the literature albeit at lower redshifts. [Lam et al. \(2019\)](#) and [Castellano et al. \(2023a\)](#) find similar slopes of the linear fit for the correlation between ξ_{ion} and

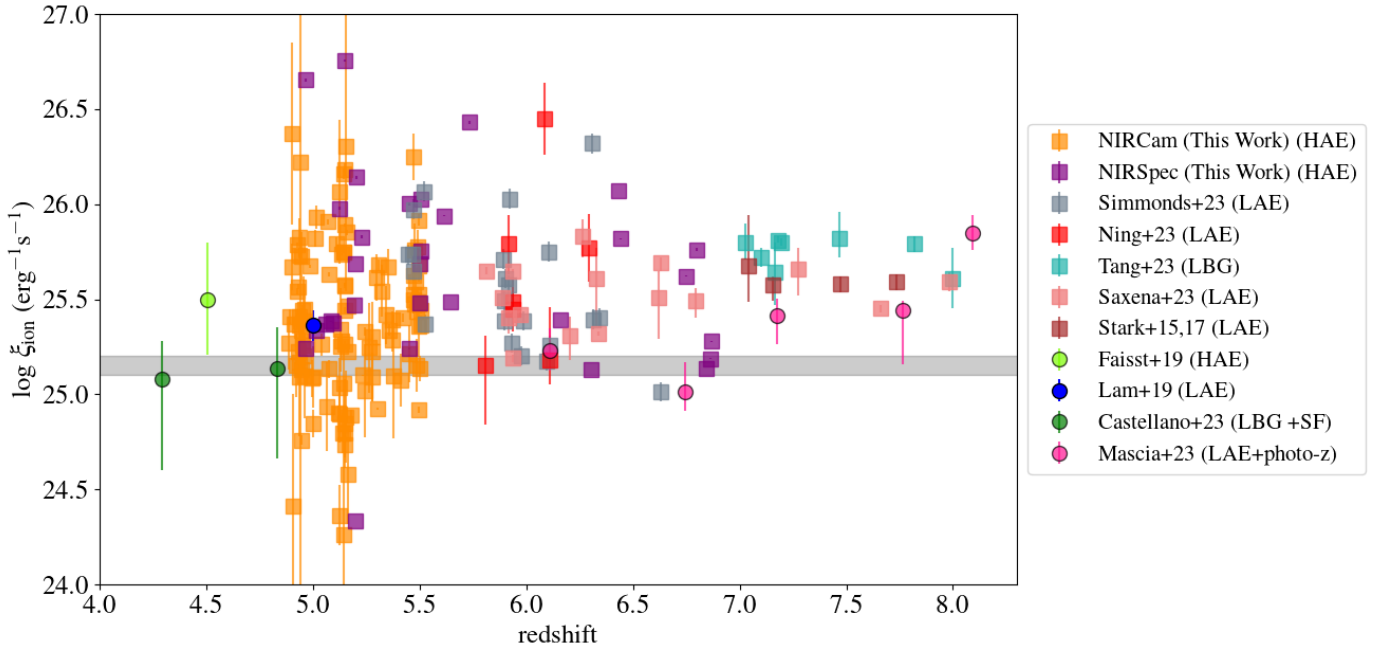


Figure 5. Evolution of the ionising photon production efficiency ξ_{ion} (uncorrected for dust) with redshift in the epoch of reionisation. The purple and orange squares of NIRSpec and NIRCam selected samples respectively are shown with various measurements of ξ_{ion} from the literature. The method of target selection is mentioned in parentheses. Circles show binned measurements of $\log \xi_{\text{ion}}$, whereas squares show individual galaxy measurements. The grey line shows the linear fit to the canonical value of ξ_{ion} required to ionise the local IGM as calculated by [Robertson et al. \(2015\)](#). There is no significant evolution of ξ_{ion} during the epoch of reionisation and the ξ_{ion} of our sample at $z < 5.5$ is comparable to their higher redshift counterparts from the literature within the errors.

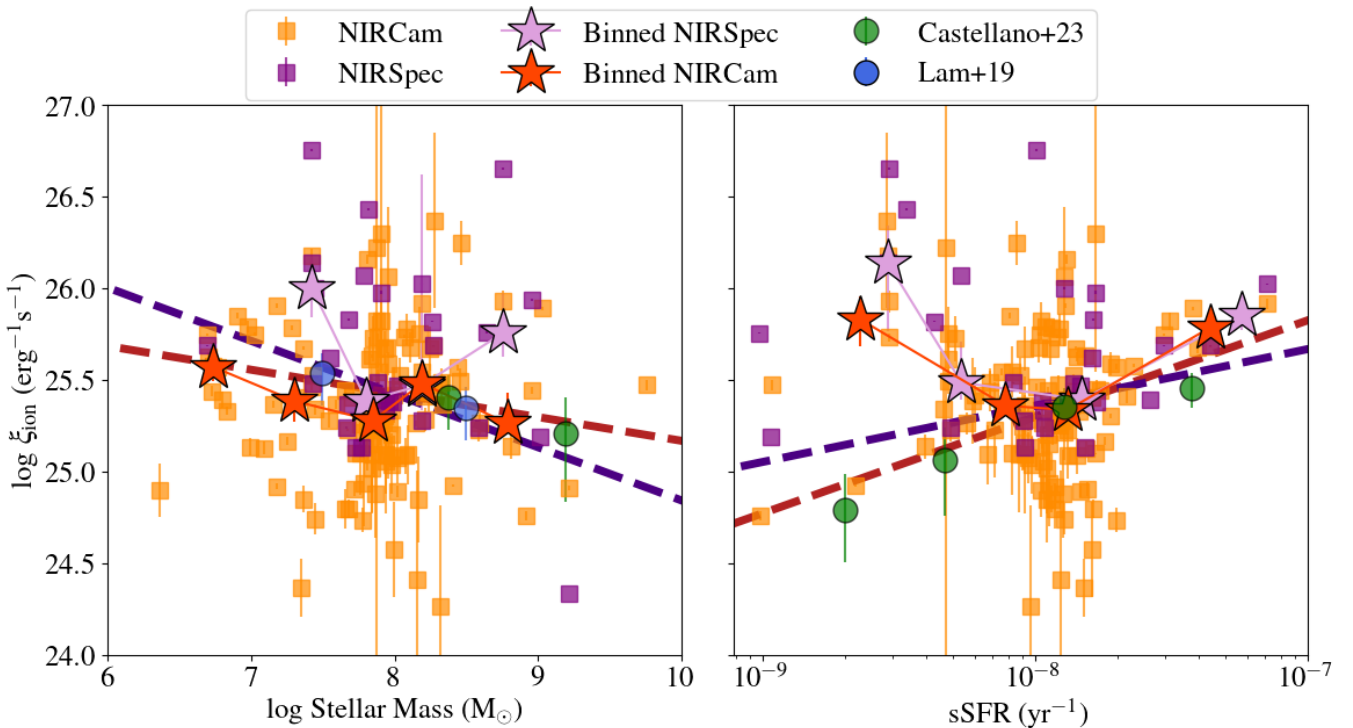


Figure 6. The ionising photon production efficiency (ξ_{ion}) as a function of stellar mass (left) and the specific star formation rate (right). The purple and orange colors show our NIRSpec and NIRCam samples respectively. The squares and stars show individual galaxies and binned samples with the lines showing linear fits to the sample. We find a moderate negative correlation of ξ_{ion} with the stellar mass of galaxies and a moderate positive correlation of ξ_{ion} with the sSFR. Dwarf star forming galaxies have a higher photon production efficiency and will require a lower escape fraction to ionise their local IGM.

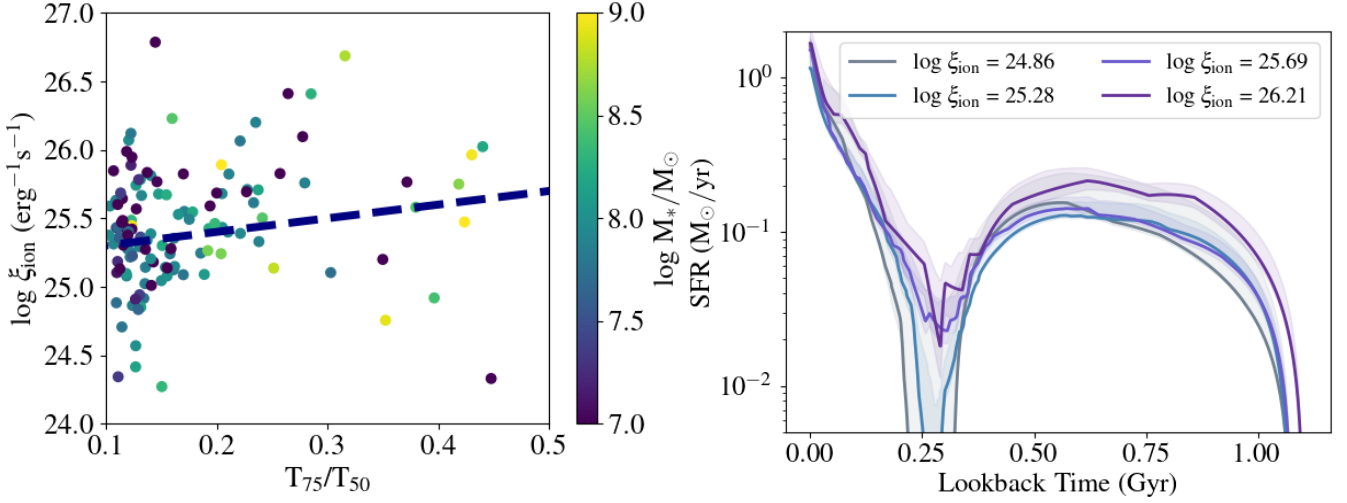


Figure 7. The ionising photon production efficiency (ξ_{ion}) is slightly positively correlated with T_{75}/T_{50} (left). A more recent burst in star formation has a smaller T_{75}/T_{50} . The markers have been color-coded with the magnification-corrected stellar mass of the galaxy. The right panel shows the star formation history of galaxies in bins of ξ_{ion} with median ξ_{ion} of the bin stated in the legend.

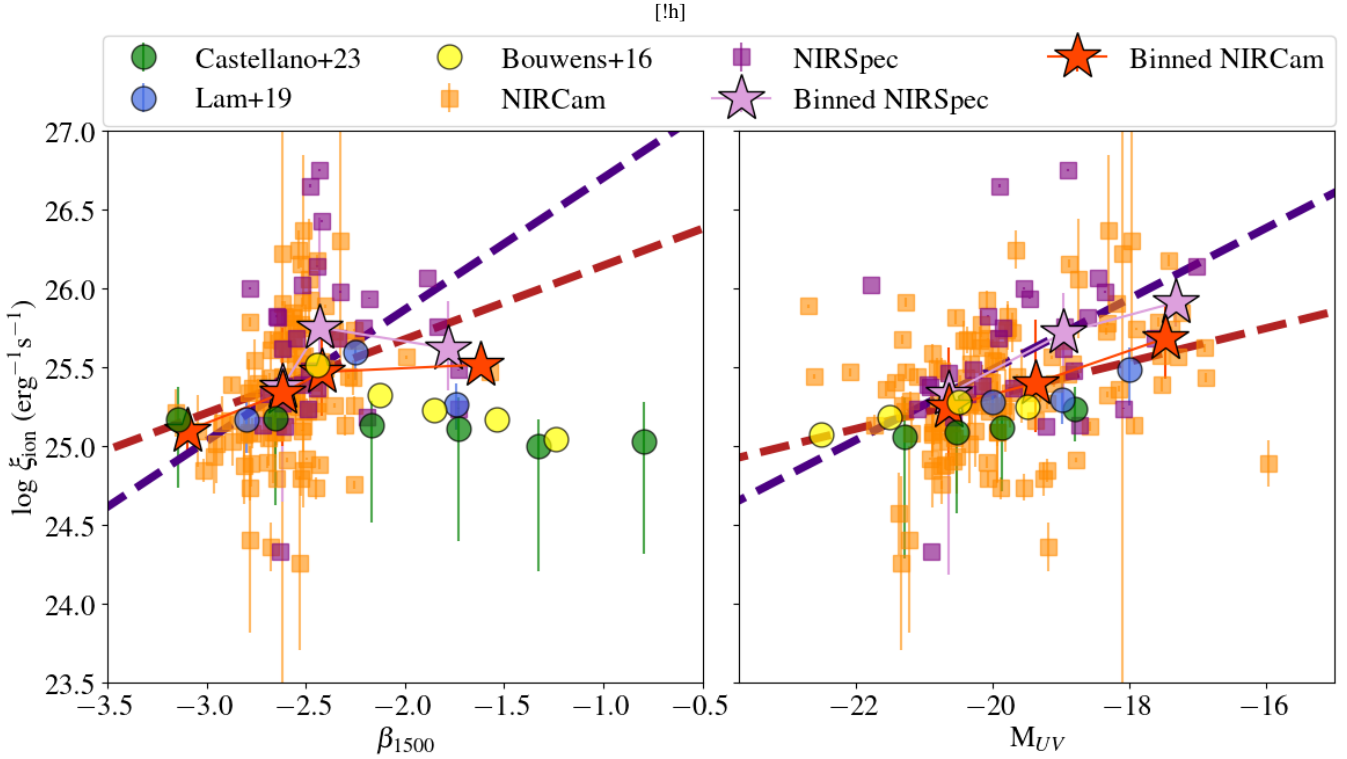


Figure 8. The ionising photon production efficiency (ξ_{ion}) as a function of UV slope (β_{1500}) (left) and the UV magnitude (M_{UV}) (right). The purple and orange colors show the NIRSpec and NIRCам samples respectively. The squares and stars show individual galaxies and binned samples with the lines showing linear fits to the sample. We find a positive correlation of ξ_{ion} with the M_{UV} in both NIRCам and NIRSpec samples similar to past studies. However, we find no significant correlation between ξ_{ion} and β_{1500} .

stellar mass at $\log M_*/M_\odot > 7$ and $\log M_*/M_\odot > 8$ at redshift ~ 5 respectively. Compared to this sample, we can extend the range of stellar mass by > 1 dex towards the lower mass end. The marginal elevation ξ_{ion} of the lower mass galaxies has important implications for the progression of ionisation and the sources of ionising photons during the epoch of reionisation. The steep slope of the faint end of the UV luminosity function at $z > 5$ (Bouwens et al. 2015; Livermore

et al. 2017; Atek et al. 2018, 2023) coupled with higher ξ_{ion} of low mass galaxies indicate such dwarf systems may emit significant ionising photons into the IGM to reionise their local environment depending on their escape fraction of ionising photons. However, we note that our sample which is biased towards high ξ_{ion} galaxies especially at the magnification uncorrected low stellar mass end due to the $H\alpha$ selection could be driving this difference.

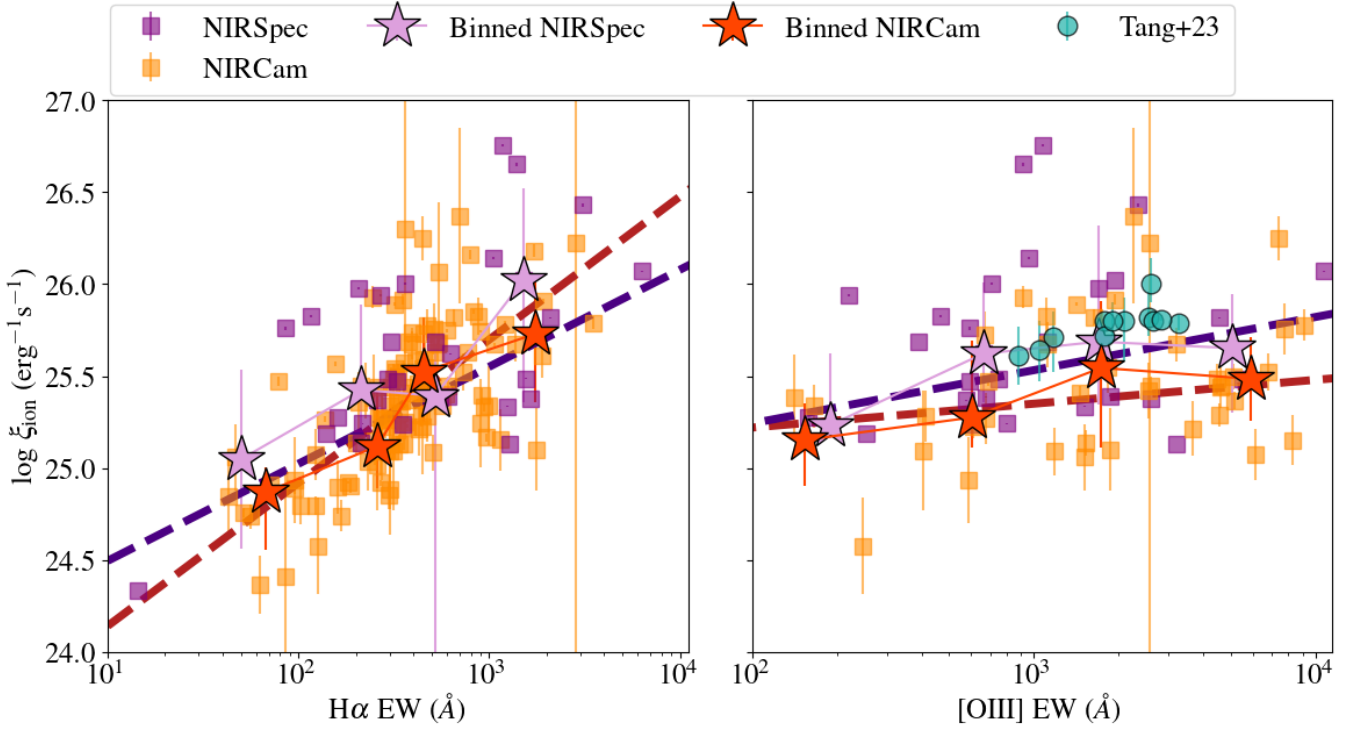


Figure 9. The ionising photon production efficiency (ξ_{ion}) as a function of $\text{H}\alpha$ equivalent width (left) and $[\text{OIII}]$ equivalent width (right). The purple and orange colors show our NIRSpec and NIRCам samples respectively. The $[\text{OIII}]$ equivalent width is only shown for the galaxies in the NCF field which have medium band observation of 5007 Å restframe wavelength. The squares and stars show individual galaxies and binned samples with the lines showing linear fits to the sample. We find a positive correlation of ξ_{ion} with the $\text{H}\alpha$ equivalent width. We also find a moderate positive correlation of ξ_{ion} with the $[\text{OIII}]$ equivalent width.

In the right panel of Figure 6, we show ξ_{ion} as a function of the specific star formation rates (sSFR) of the galaxies as measured from SED fitting (refer to section 3.1 for the description of SED fitting). We note that both ξ_{ion} and sSFR are not affected by magnification correction. Our samples cover a range of $\log \text{sSFR} = -9$ to -7 yr^{-1} . Similar to the stellar mass, we have binned the sample in sSFR and the stars depict the median ξ_{ion} vs the median sSFR of the binned sample. We bin the sample with $\log \text{sSFR} = -9$ to -8.5 , -8.5 to -8 , -8 to -7.5 and $> -7.5 \text{ yr}^{-1}$. In both the NIRCам and NIRSpec samples, we find a positive correlation between ξ_{ion} and sSFR with slope of the linear fit 0.48 for the NIRCам sample and 0.29 for the NIRSpec sample. However, we also find a small sub-sample of outliers to this correlation at the low sSFR end ($\log \text{sSFR} < -8.5 \text{ yr}^{-1}$). This low sSFR end of our sample ($\sim 10\%$ of the sample) shows a larger scatter and higher median ξ_{ion} . This difference could be a result of the $\text{H}\alpha$ selection, which would bias our sample to higher ξ_{ion} , especially at low sSFR. We note that between $\log \text{sSFR} -8.5$ to -7.5 , where $\sim 85\%$ of the sample lies, we find no significant correlation of ξ_{ion} but a large intrinsic scatter of $\sigma = 0.38$. We further calculate the Spearman coefficient of -0.06 and -0.13 for correlation between ξ_{ion} and $\log \text{sSFR}$ for the NIRCам sample and the NIRSpec sample respectively. Although the linear fit and the Spearman coefficient point towards a slight positive correlation between ξ_{ion} and the sSFR of a galaxy, we note that these results have high intrinsic scatter and do not show a clear correlation.

We compare our results with [Castellano et al. \(2023b\)](#), who find a very significant monotonically increasing correlation between ξ_{ion} and sSFR of galaxies at $2 < z < 5$. They report that the ξ_{ion} increases from $\log \xi_{\text{ion}} = 24.5 \text{ Hz erg}^{-1}$ at $\log \text{sSFR} = -9.5 \text{ yr}^{-1}$

to $= 25.5 \text{ Hz erg}^{-1}$ at $\log \text{sSFR} = -7.5 \text{ yr}^{-1}$. They also found a Spearman correlation coefficient of ~ 0.79 compared to 0.013 and a large p-value of 0.5 in our sample. Similar to our results, [Castellano et al. \(2023b\)](#) also find a larger scatter of ξ_{ion} at the lower end of sSFR indicating a lower correlation of ξ_{ion} with sSFR at the low sSFR end, however, unlike our result, the median ξ_{ion} at the lower sSFR is lower than ξ_{ion} at the higher sSFR end. The difference in the results could be driven by the $\text{H}\alpha$ selection or could also be explained by the redshift evolution of the median sSFR of the galaxies indicating that at $z > 5$, ξ_{ion} is not highly correlated to the sSFR of the galaxy as galaxies may have a stochastic star formation history which will rapidly fluctuate the sSFR of a galaxy.

Given the possible effect of stochasticity, we explore further the time scales with which ξ_{ion} changes with the star formation by studying the correlation of ξ_{ion} with stellar ages and star formation histories. We derive the times when the galaxy creates 50% and 75% of its stellar mass (T_{50} and T_{75} , at the time of observation) using the non-parametric histories of Dense Basis SED fitting. Figure 7 shows ξ_{ion} as a function of the ratio T_{75}/T_{50} (left panel) with each galaxy colored by its stellar mass. The ratio T_{75}/T_{50} is indicative of the relative time of the last burst of star formation in the galaxy such that a lower T_{75}/T_{50} indicates a more recent burst. We find a moderate positive correlation between ξ_{ion} and $T_{50}/T_{75} < 0.3$ such that ξ_{ion} is decreasing on average with more recent bursts. However, we find a small sample of galaxies with $T_{50}/T_{75} > 0.3$ that have a lower median ξ_{ion} . This indicates a potential correlation of ξ_{ion} with the age of the starburst, however, we note that the effect is also dependent on the star formation history and the strength of the starburst. We also find the lowest stellar mass galaxies have had a more recent burst

compared to the more massive galaxies in our sample. We note that the $H\alpha$ selection biases our sample to galaxies with ongoing active star formation i.e. either to a rising or bursty star formation history.

We further divide our sample into ξ_{ion} bins and plot their median star formation histories (right panel, figure 7). The median ξ_{ion} of each bin and their respective medians magnification corrected stellar masses are: $\log \xi_{\text{ion}} = 24.86 \pm 0.05, 25.28 \pm 0.02, 25.69 \pm 0.02, 26.21 \pm 0.04$ and $\log M_*/M_\odot = 7.78 \pm 0.14, 7.89 \pm 0.07, 7.88 \pm 0.1, 7.90 \pm 0.12$. We find that on average our sample is experiencing an ongoing star formation burst. However, this could be a result of the selection of $H\alpha$ emitters exclusively. The bin with the highest ξ_{ion} started the burst < 100 Myrs earlier than the lowest ξ_{ion} bin. Thus, we infer that there may be a potential delay of increase in the production rate of ionising photons from the start of the last rise in star formation.

4.2.3 ξ_{ion} vs UV properties

In this section, we study the correlation of UV properties with ξ_{ion} . In figure 8, we show ξ_{ion} as a function of the UV slope (β_{1500} , left panel) and the UV magnitude (M_{UV} , right panel). We find that ξ_{ion} correlates positively with β_{1500} in our NIRCcam sample with slope = 0.49 and the Spearman correlation coefficient = 0.32. Similarly, ξ_{ion} correlates positively with β_{1500} with slope of 0.5 in our NIRSpec sample. However, the β_{1500} measurement from EAZY SED fitting recovers β_{1500} in a small range ($-3.1 < \beta_{1500} < 2$), and we find a significant scatter of ξ_{ion} within this range. Compared to other studies, Bouwens et al. (2016) and Castellano et al. (2023b) find a negative correlation of β_{1500} with ξ_{ion} , whereas Lam et al. (2019) find no significant correlation. From the variability of β_{1500} with measurement and the difference in results across literature, we infer that ξ_{ion} is not correlated with β_{1500} at $z > 5$.

We measure the correlation between ξ_{ion} and the M_{UV} . We find a positive correlation with a slope and Spearman correlation coefficients of 0.16 and 0.34 in our NIRCcam sample, and 0.18 and 0.61 in our NIRSpec sample. We find a steeper correlation between ξ_{ion} and M_{UV} compared to Bouwens et al. (2016), Castellano et al. (2023b) and Lam et al. (2019). We are able to increase the range of M_{UV} towards the faint end to ~ -16 and our result indicates a higher production rate of ionising photons for UV faint galaxies compared to other studies.

4.3 Ionisation Conditions from restframe Emission Lines

The ionising photon production efficiency depends on the star formation and the ionising conditions of the galaxy ISM. In this section, we study the correlation between ξ_{ion} and $H\alpha$ and [OIII]+H β equivalent widths which trace the average stellar ages and the ionisation parameter of the ISM respectively. Figure 9 shows ξ_{ion} as a function of $H\alpha$ EW (left) and [OIII]+H β EW (right). ξ_{ion} is highly correlated with $H\alpha$ EW in both NIRCcam (slope 0.7, Spearman coefficient 0.6) and NIRSpec (slope 0.5, Spearman coefficient 0.5) samples. Although partially the correlation found is driven by the fact that ξ_{ion} is measured with $H\alpha$ luminosity, ξ_{ion} is also dependent on UV luminosity, and $H\alpha$ EW is dependent on the strength of the stellar continuum as well. Our results are comparable with Atek et al. (2022), who find a correlation with a slope of 0.63 for low stellar mass galaxies at $z \sim 1$ and other studies at low redshifts ($z \sim 1-2$) (Emami et al. 2020; Tang et al. 2019; Matthee et al. 2016).

At lower redshifts ($z \sim 1-2$), ξ_{ion} is known to correlate with the [OIII]+H β EW (Chevallard et al. 2018; Tang et al. 2019; Onodera

et al. 2020). At higher redshifts Tang et al. (2023) show for a small sample of $z > 7$ galaxies that the ξ_{ion} is similarly correlated with [OIII]+H β EW and also that [OIII]+H β EW is correlated with the O32 ratio which traces the ionisation parameter of the galaxy ISM. Here we investigate the correlation of ξ_{ion} [OIII]+H β EW in our NIRSpec and NIRCcam (only in the NCF field) samples. We find that, ξ_{ion} is moderately correlated with [OIII]+H β EW in the NIRCcam sample (slope 0.12, Spearman coefficient 0.5) and with [OIII] EW in the NIRSpec sample (slope 0.4, Spearman coefficient 0.3). This result is consistent with the correlation found in both lower and higher redshift samples (Chevallard et al. 2018; Tang et al. 2019; Onodera et al. 2020; Tang et al. 2023). In conjunction with the result in Tang et al. (2023), this indicates that ξ_{ion} is correlated with the ionisation parameter of the galaxy.

In the NIRCcam sample, we find median [OIII]+H β EW = $1861 \pm 433 \text{ \AA}$ which is comparable to $1993 \pm 214 \text{ \AA}$ for [OIII] emitters at $z \sim 8$ (Tang et al. 2023) but higher than the $\sim 700 \text{ \AA}$ at $z \sim 6$ found in Endsley et al. (2023a). The higher [OIII]+H β EW in our sample compared to Endsley et al. (2023a) could be driven by our $H\alpha$ selection which biases the sample towards higher star forming and hence emission line galaxies. In our NIRSpec sample, we find a median [OIII] EW of $802 \pm 360 \text{ \AA}$ which is higher compared to the lower redshift sample ($\sim 100 \text{ \AA}$ for star forming galaxies at $z = 2$ (Reddy et al. 2018)), but similar to the [OIII] EWs in extreme emission line galaxies at $z \sim 3$ (Gupta et al. 2023).

Further, we investigate the correlation of $H\alpha$ and [OIII]+H β EWs with the UV magnitude shown in figure 10. We find a positive correlation between $H\alpha$ and the M_{UV} in the NIRCcam sample with a slope of 0.12 and a Spearman correlation coefficient of 0.41 with a very small p-value indicating a strong correlation. However, we find no significant correlation between $H\alpha$ and the M_{UV} in the NIRSpec sample with 0 slope and a large p-value for the Spearman correlation coefficient. The difference in correlation of $H\alpha$ with M_{UV} between the NIRSpec and NIRCcam sample might be driven by the $H\alpha$ selection and shallower depth of the NIRSpec sample compared to the NIRCcam sample. We note that at $M_{\text{UV}} < -18$, we also find a large scatter in $H\alpha$ (median $H\alpha$ EW = 339.27 \AA and $\sigma = 1651.06 \text{ \AA}$) compared to the fainter end ($M_{\text{UV}} > -18$; median $H\alpha$ EW = 517.8 \AA and $\sigma = 794.69 \text{ \AA}$). Although the UV faint sample ($M_{\text{UV}} > -18$) has been magnified due to gravitational lensing from the foreground cluster, $H\alpha$ EW is independent of the magnification. Our results are comparable to the median $H\alpha$ EW ($\approx 400 \text{ \AA}$) found in previous studies (Faist et al. 2019; Lam et al. 2019). However, we report a lower median $H\alpha$ EW compared to EW reported in Endsley et al. (2023b), who also do not find a correlation between $H\alpha$ EW and M_{UV} in the Lyman break selected galaxies.

Figure 10 shows the correlation between [OIII]+H β EW and the UV magnitude. We find no significant correlation between [OIII]+H β EW in the bright UV sample ($M_{\text{UV}} < -18$). Due to the lack of medium bands observations of the [OIII]+H β emission in the CLU field which are magnified due to gravitational lensing, we are limited to the $M_{\text{UV}} < -18$ sample. Within the range $-23 < M_{\text{UV}} < -18$, we find a median [OIII]+H β EW = 917.27 \AA and a large scatter of $\sigma = 2621.65 \text{ \AA}$. We also do not find a correlation between [OIII]+H β EW and the UV magnitude with 0 slope and large p-value for Spearman correlation coefficients. Similar to previous studies, we find a large [OIII]+H β EW compared to $z \sim 2$, and 46 extreme emission galaxies with $> 1200 \text{ \AA}$ [OIII]+H β EW. The median [OIII]+H β EW of our NIRCcam sample is lower than 1994 \AA reported in Tang et al. (2023) for $z > 7$ galaxies but higher than median [OIII]+H β EW ($< 890 \pm 60 \text{ \AA}$) reported in Endsley et al. (2023b). Endsley et al. (2023b) also find that the UV faint ($M_{\text{UV}} > -19$) galaxies have a lower [OIII]+H β

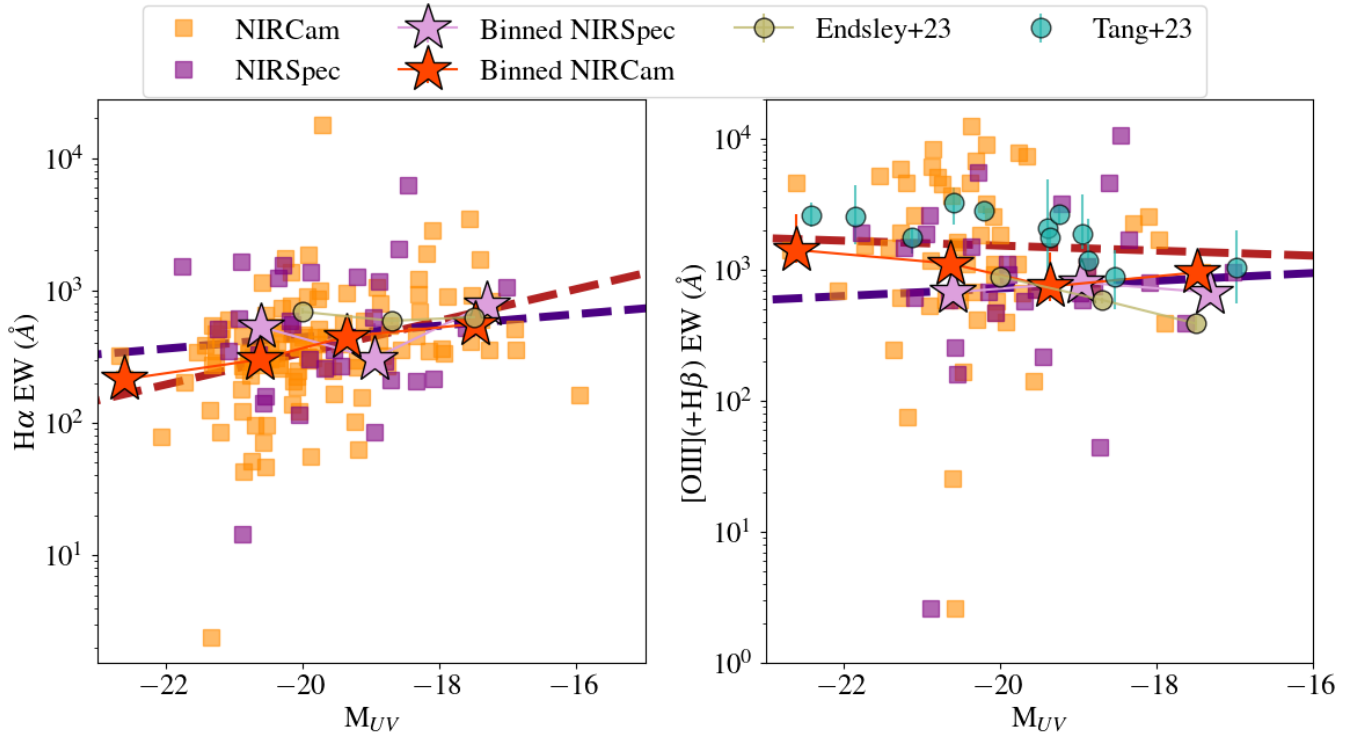


Figure 10. $H\alpha$ equivalent width (left) and $[OIII](+H\beta)$ equivalent widths (right) as a function of UV magnitude. The purple and orange colors show our NIRSpec and NIRCam samples respectively. The $[OIII]$ equivalent width is shown for the NIRSpec sample and $[OIII]+H\beta$ EW for galaxies in the NCF field which have medium band observation of 5007 \AA restframe wavelength. The squares and stars show individual galaxies and binned samples with the lines showing linear fits to the sample. We find a positive correlation of $H\alpha$ EW with the UV magnitude and no significant correlation of $[OIII](+H\beta)$ EW with the UV magnitude.

EW which is driven by lower metallicities as well as more recently-declining star formation histories relative. However, in our sample, we find that the UV faint ($M_{UV} > -19$) galaxies have a higher $H\alpha$ EW which indicates lower metallicities and high star formation rates. The difference in trends compared to Endsley et al. (2023b) could arise from differences in sample selection strategies, where we have selected galaxies with F410M band excess that biases our sample towards star forming galaxies with higher nebular emission, whereas Endsley et al. (2023b) follow a Lyman-break selection which allows them to select galaxies that are not biased towards higher emission.

5 CONCLUSIONS

In this work, we present the UV and ionisation properties and star formation of dwarf galaxies at $z \sim 5$ to 7. We use the CANUCS NIRCam and NIRSpec observations of the MACS0417 CLU field and the respective NCF field. Our sample is selected with a F410M band flux excess at $4.8 < z < 5.5$ such that the $H\alpha$ emission is included in the medium band and we can measure accurate emission line flux and EWs. We confirm the line fluxes for a subset of the NIRCam sample with NIRSpec follow-up (figure 2). With the magnification from the foreground cluster scale lens in our field, we are also able to push to fainter and lower mass galaxies compared to previous studies at similar redshifts. Using this data, we discussed the evolution of β_{1500} and ξ_{ion} and their dependence on the galaxy properties and star formation histories. We also study the ionising properties of our sample using emission line EWs. We summarise our results as follows:

1. We find bluer UV slopes of dwarf galaxies with median

$\beta_{1500} -2.56 \pm 0.26$ in the NIRCam sample. We find no significant evolution of β_{1500} with redshift during the epoch of reionisation but find a significant correlation between β_{1500} and the stellar mass of the galaxy in both our sample sets. These results indicate a lack of dust build-up or a higher presence of ionising radiation in star forming dwarf galaxies at $z \sim 5$.

2. We do not find any evolution of ξ_{ion} with redshift in the EoR and no significant difference between ξ_{ion} of $Ly\alpha$ emitters reported in the literature with our sample (median $\log \xi_{ion} = 25.36 \pm 0.04$ and 25.49 ± 0.18 in NIRCam and NIRSpec samples respectively, figure 5). The median $\log \xi_{ion}$ of our sample sets is also above the canonical value of 25.2 required to reionise the local IGM with approximately 20% escape fraction (Robertson et al. 2015). The lack of difference between the median ξ_{ion} $Ly\alpha$ emitters and non-emitters indicates different physical processes affecting the production of ionising photons and the creation of escape channels for Lyman α photons.

3. We find a moderate correlation of ξ_{ion} with the stellar mass and the specific star formation rates in a galaxy, such that ξ_{ion} decreases with increasing stellar mass and increases with increasing sSFR (figure 6). On further investigation of the star formation histories, we find that the majority of our $H\alpha$ selected galaxies are undergoing recent star formation raise/burst which creates a large scatter in the ξ_{ion} . We also find that the relative time of burst is correlated to average ξ_{ion} and indicates a delay in of ≈ 50 Myrs between the final rise in star formation/burst and increasing ξ_{ion} (figure 7).

4. We investigate the correlation between ξ_{ion} and UV properties β_{1500} and M_{UV} . We find a significant correlation between M_{UV} and ξ_{ion} such that ξ_{ion} increases with decreasing M_{UV} . This implies a possible greater contribution of UV faint and dwarf galaxies to reionising the Universe. However, we find no significant and opposite

correlation between β_{1500} and ξ_{ion} . The NIRCcam sample, which covers a small dynamic range of beta finds higher ξ_{ion} for redder β_{1500} . The large scatter in β_{1500} and ξ_{ion} which arise due to the stochastic nature of star formation histories in dwarf galaxies could explain the observed discrepancy.

5. We also find a significant correlation between ξ_{ion} and EWs of restframe optical emission lines. We find that ξ_{ion} increases highly with increasing $H\alpha$ EW and moderately with [OIII]+ $H\beta$ EW. We further explore the correlation of restframe optical emission EWs with M_{UV} . We find that on average $H\alpha$ EW increases with M_{UV} , although our bright end of the M_{UV} range has a high scatter in $H\alpha$ EW indicating a stochastic star formation history with very recent bursts. However, our UV faint sample shows a high $H\alpha$ EW. On the other hand, we do not find a significant correlation between [OIII]+ $H\beta$ EW and M_{UV} . However, the lack of medium band observation covering the [OIII]+ $H\beta$ emission in the CLU field limits us to $M_{\text{UV}} < -18$, where we similarly find a large scatter in [OIII]+ $H\beta$ EW.

Our results from one of the five cluster fields of CANCUS provide a large set of empirical measurements of UV and ionising properties of dwarf star forming galaxies at $z > 5$. We demonstrate here the use of medium band photometry to accurately derive emission line fluxes without having to rely solely on spectroscopy. Similar studies characterising the properties of dwarf galaxies across the epoch of reionisation are required to fully understand how reionisation of the Universe progressed. This work will be supplemented by future studies with the full CANUCS data at $z > 5$, which will provide a better understanding of the general population of galaxies across the history of the Universe.

ACKNOWLEDGEMENTS

AH, MB, GR, and NM acknowledge support from the ERC Grant FIRSTLIGHT and Slovenian national research agency ARRS through grants N1-0238 and P1-0188. MB acknowledges support from the program HST-GO-16667, provided through a grant from the STScI under NASA contract NAS5-26555. This research was enabled by grant 18JWST-GTO1 from the Canadian Space Agency and funding from the Natural Sciences and Engineering Research Council of Canada. This research used the Canadian Advanced Network For Astronomy Research (CANFAR) operated in partnership by the Canadian Astronomy Data Centre and The Digital Research Alliance of Canada with support from the National Research Council of Canada the Canadian Space Agency, CANARIE and the Canadian Foundation for Innovation. The Cosmic Dawn Center (DAWN) is funded by the Danish National Research Foundation under grant No. 140.

DATA AVAILABILITY

Raw JWST data used in this work is available from the Mikulski Archive for Space Telescopes (<https://archive.stsci.edu>; doi: 10.17909/ph4n-6n76). Processed data products will be available on <http://canucs-jwst.com>.

REFERENCES

Alcorn L. Y., et al., 2019, *The Astrophysical Journal*, 883, 153
 Anderson L., Governato F., Karcher M., Quinn T., Wadsley J., 2017, *Monthly Notices of the Royal Astronomical Society*, 468, 4077

Asada Y., et al., 2024, *MNRAS*, 527, 11372
 Atek H., Richard J., Kneib J. P., Schaerer D., 2018, *Monthly Notices of the Royal Astronomical Society*, 479, 5184
 Atek H., Furtak L. J., Oesch P., Dokkum P. V., Reddy N., Contini T., Illingworth G., Wilkins S., 2022, *Monthly Notices of the Royal Astronomical Society*, 511, 4464
 Atek H., et al., 2023
 Balu S., Greig B., Qiu Y., Power C., Qin Y., Mutch S., Wyithe J. S. B., 2023, *MNRAS*, 520, 3368
 Bhatawdekar R., Conselice C. J., Margalef-Bentabol B., Duncan K., 2018, [10.1093/mnras/stz866](https://arxiv.org/abs/10.1093/mnras/stz866)
 Bolan P., et al., 2021, [10.1093/mnras/stac1963](https://arxiv.org/abs/10.1093/mnras/stac1963)
 Bouwens R. J., et al., 2011, [10.1088/2041-8205/752/1/L5](https://arxiv.org/abs/10.1088/2041-8205/752/1/L5)
 Bouwens R. J., et al., 2014, [10.1088/0004-637X/803/1/34](https://arxiv.org/abs/10.1088/0004-637X/803/1/34)
 Bouwens R. J., Illingworth G. D., Oesch P. A., Caruana J., Holwerda B., Smit R., Wilkins S., 2015, *Astrophysical Journal*, 811
 Bouwens R. J., Smit R., Labbe I., Franx M., Caruana J., Oesch P., Stefanon M., Rasappu N., 2016, *The Astrophysical Journal*, 831, 176
 Bradley L., et al., 2022, astropy/photutils: 1.6.0, Zenodo, doi:10.5281/zenodo.7419741
 Brammer G., 2023a, eazy-py, Zenodo, doi:10.5281/zenodo.5012704
 Brammer G., 2023b, msaexp: NIRSpc analysis tools, Zenodo, doi:10.5281/zenodo.7299500
 Brammer G., Matharu J., 2021, gbrammer/grizli: Release 2021, Zenodo, doi:10.5281/zenodo.5012699
 Brammer G. B., van Dokkum P. G., Coppi P., 2008, *The Astrophysical Journal*, 686, 1503
 Byler N., 2018, nell-byler/cloudyfsps: Initial release of cloudyFSPS, Zenodo, doi:10.5281/zenodo.1156412
 Calzetti D., Kinney A. L., Storchi-Bergmann T., 1994, *ApJ*, 429, 582
 Calzetti D., Armus L., Bohlin R. C., Kinney A. L., Koornneef J., 2000, THE DUST CONTENT AND OPACITY OF ACTIVELY STAR-FORMING GALAXIES I THAISA STORCHI-BERGMANN
 Cameron A. J., et al., 2023, *Astronomy & Astrophysics*, 677, A115
 Castellano M., et al., 2023a, [10.1051/0004-6361/202346069](https://arxiv.org/abs/10.1051/0004-6361/202346069)
 Castellano M., et al., 2023b, [10.1051/0004-6361/202346069](https://arxiv.org/abs/10.1051/0004-6361/202346069)
 Chabrier G., 2003, *Publications of the Astronomical Society of the Pacific*, 115, 763
 Chevallard J., et al., 2018, *Monthly Notices of the Royal Astronomical Society*, 479, 3264
 Chisholm J., et al., 2022, [10.1093/mnras/stac2874](https://arxiv.org/abs/10.1093/mnras/stac2874)
 Coil A. L., et al., 2014, [10.1088/0004-637X/801/1/35](https://arxiv.org/abs/10.1088/0004-637X/801/1/35)
 Conroy C., Gunn J. E., 2010, FSPS: Flexible Stellar Population Synthesis, Astrophysics Source Code Library, record ascl:1010.043 (ascl:1010.043)
 Davies F. B., et al., 2018, *The Astrophysical Journal*
 Dressler A., Henry A., Martin C. L., Sawicki M., McCarthy P., Villaneuva E., 2015, *Astrophysical Journal*, 806
 Duncan K., Conselice C. J., 2015, *Monthly Notices of the Royal Astronomical Society*, 451, 2030
 Eisenstein D. J., et al., 2023, *arXiv e-prints*, p. arXiv:2306.02465
 Eldridge J. J., et al., 2017, [10.1017/pasa.2017.51](https://arxiv.org/abs/10.1017/pasa.2017.51)
 Emami N., Siana B., Alavi A., Gburek T., Freeman W. R., Richard J., Weisz D. R., Stark D. P., 2020, *The Astrophysical Journal*, 895, 116
 Endsley R., et al., 2023a
 Endsley R., et al., 2023b
 Erb D. K., 2015, Feedback in low-mass galaxies in the early Universe, doi:10.1038/nature14454
 Faisst A. L., Capak P. L., Emami N., Tacchella S., Larson K. L., 2019, [10.3847/1538-4357/ab425b](https://arxiv.org/abs/10.3847/1538-4357/ab425b)
 Ferland G. J., et al., 2017
 Finkelstein S. L., et al., 2015, *Astrophysical Journal*, 810
 Finkelstein S. L., et al., 2019, [10.3847/1538-4357/ab1ea8](https://arxiv.org/abs/10.3847/1538-4357/ab1ea8)
 Gupta A., et al., 2023, *MNRAS*, 519, 980
 Ishigaki M., Kawamata R., Ouchi M., Oguri M., Shimasaku K., Ono Y., 2015, *Astrophysical Journal*, 799
 Iyer K., Gawiser E., 2017, *The Astrophysical Journal*, 838, 127
 Iyer K. G., Gawiser E., Faber S. M., Ferguson H. C., Kartaltepe J., Koekemoer

- A. M., Pacifici C., Somerville R. S., 2019, *The Astrophysical Journal*, 879, 116
- Jiang L., Cohen S. H., Windhorst R. A., Egami E., Finlator K., Schaerer D., Sun F., 2020, *The Astrophysical Journal*, 889, 90
- Jullo E., Kneib J. P., Limousin M., Elasdttir A., Marshall P.J., Verdugo T., 2007, *New Journal of Physics*, 9
- Karman W., et al., 2016, [10.1051/0004-6361/201629055](https://doi.org/10.1051/0004-6361/201629055)
- Kneib J. P., Mellier Y., Fort B., Mathez G., 1993, *A&A*, 273, 367
- Lam D., et al., 2019, *Astronomy and Astrophysics*, 627
- Larson R. L., et al., 2022
- Leitherer C., Heckman T. M., 1995, SYNTHETIC PROPERTIES OF STAR-BURST GALAXIES
- Lin Y.-H., et al., 2023
- Livermore R. C., Finkelstein S. L., Lotz J. M., 2017, *The Astrophysical Journal*, 835, 113
- Mahler G., et al., 2019, *The Astrophysical Journal*, 873, 96
- Markov V., Gallerani S., Ferrara A., Pallottini A., Parlanti E., Di Mascia F., Sommovigo L., Kohandel M., 2024, [arXiv e-prints](https://arxiv.org/abs/2402.05996), p. [arXiv:2402.05996](https://arxiv.org/abs/2402.05996)
- Mascia S., et al., 2023
- Matthee J., Sobral D., Best P., Khostovan A. A., Oteo I., Bouwens R., Rattgering H., 2016, [10.1093/mnras/stw2973](https://doi.org/10.1093/mnras/stw2973)
- Matthee J., Mackenzie R., Simcoe R. A., Kashino D., Lilly S. J., Bordoloi R., Eilers A.-C., 2023, *The Astrophysical Journal*, 950, 67
- McGreer I., Mesinger A., D'Odorico V., 2014, [10.1093/mnras/stu2449](https://doi.org/10.1093/mnras/stu2449)
- Mehta V., et al., 2017, *The Astrophysical Journal*, 838, 29
- Naidu R. P., Tacchella S., Mason C. A., Bose S., Oesch P. A., Conroy C., 2019, [10.3847/1538-4357/ab7cc9](https://doi.org/10.3847/1538-4357/ab7cc9)
- Nakajima K., Ellis R. S., Iwata I., Inoue A. K., Kusakabe H., Ouchi M., Robertson B. E., 2016, [10.3847/2041-8205/831/1/L9](https://doi.org/10.3847/2041-8205/831/1/L9)
- Nanayakkara T., et al., 2020, [10.3847/1538-4357/ab65eb](https://doi.org/10.3847/1538-4357/ab65eb)
- Nanayakkara T., et al., 2023, *The Astrophysical Journal Letters*, 947, L26
- Ning Y., Cai Z., Jiang L., Lin X., Fu S., Spinoso D., 2022, [10.3847/2041-8213/acb26b](https://doi.org/10.3847/2041-8213/acb26b)
- Noirot G., et al., 2023, *Monthly Notices of the Royal Astronomical Society*, 525, 1867
- Onodera M., et al., 2020, *The Astrophysical Journal*, 904, 180
- Osterbrock D. E., 1989, Astrophysics of gaseous nebulae and active galactic nuclei
- Ouchi M., et al., 2009, [10.1088/0004-637X/706/2/1136](https://doi.org/10.1088/0004-637X/706/2/1136)
- Paardekooper J.-P., Khochfar S., Vecchia C. D., 2012, [10.1093/mnras/1sls032](https://doi.org/10.1093/mnras/1sls032)
- Prieto-Lyon G., et al., 2022, [10.1051/0004-6361/202245532](https://doi.org/10.1051/0004-6361/202245532)
- Reddy N. A., Steidel C. C., 2009, *Astrophysical Journal*, 692, 778
- Reddy N. A., et al., 2018, *The Astrophysical Journal*, 869, 92
- Robertson B. E., 2022, *ARA&A*, 60, 121
- Robertson B. E., Ellis R. S., Furlanetto S. R., Dunlop J. S., 2015, [10.1088/2041-8205/802/2/L19](https://doi.org/10.1088/2041-8205/802/2/L19)
- Sawicki M., Thompson D., 2006, KECK DEEP FIELDS. III. LUMINOSITY-DEPENDENT EVOLUTION OF THE ULTRAVIOLET LUMINOSITY AND STAR FORMATION RATE DENSITIES AT $z \approx 4, 3$, AND 2
- Saxena A., et al., 2023
- Simmonds C., et al., 2023
- Stefanon M., et al., 2019, *ApJ*, 883, 99
- Stefanon M., Bouwens R. J., Illingworth G. D., Labbe I., Oesch P. A., Gonzalez V., 2022, *The Astrophysical Journal*, 935, 94
- Tang M., Stark D. P., Chevallard J., Charlot S., 2019, *Monthly Notices of the Royal Astronomical Society*, 489, 2572
- Tang M., et al., 2023
- Topping M. W., et al., 2023
- Vilella-Rojo G., et al., 2015, *Astronomy and Astrophysics*, 580
- Willott C. J., et al., 2022, *Publications of the Astronomical Society of the Pacific*, 134
- Wise J. H., Demchenko V. G., Halicek M. T., Norman M. L., Turk M. J., Abel T., Smith B. D., 2014, [10.1093/mnras/stu979](https://doi.org/10.1093/mnras/stu979)
- Yamanaka S., Yamada T., 2019, *PASJ*, 71, 51

This paper has been typeset from a $\text{\TeX}/\text{\LaTeX}$ file prepared by the author.